Accuracy of Non-linear Finite Element Modelling for Surgical Simulation: Study Using Brain Phantom

Jiajie Ma, Adam Wittek, Karol Miller

Intelligent Systems for Medicine Laboratory
School of Mechanical Engineering
The University of Western Australia
35 Stirling Highway
Crawley WA 6009, Australia
Phone: + (61) 8 6488 7815
Fax: + (61) 8 6488 1024
Email: majiajie@mech.uwa.edu.au

Http://www.mech.uwa.edu.au/ISML/

Abstract

In this study, we evaluated the accuracy of non-linear finite element analysis in surgical simulation through its application in modelling of indentation of the human brain phantom. The phantom was moulded from a silicone gel, a brain tissue substitute material widely used in mechanical head models. The evaluation was done in terms of the finite element model ability to predict the forces acting on the indenter and phantom deformation due to these forces. Deformation field within the phantom was determined by tracking 3D motions of the X-ray opaque markers implanted within the phantom. The brain phantom model was implemented using the ABAQUS finite element solver. Accurate geometry for the model was obtained through MRI scans of the phantom. The specific constitutive properties for the model were determined using uniaxial compression of the phantom material samples. The computational grid (i.e. finite element mesh) was built using second order tetrahedron elements with mixed formulation that prevents volumetric locking. The model predicted the indentation force with an error of only 5%. The phantom deformation was predicted with an average error of 0.3186 mm which is within the uncertainty (0.359 mm) of the experimental measurements of the X-ray markers displacement. Such excellent agreement between the modelling and experimental results indicates high predictive power of the non-linear finite element modelling in surgical simulation.

Keywords: surgical simulation, non-linear finite element modelling, brain phantom, soft tissue deformation, predictive power, bi-plane XRII system.

Table of Content

1.Introduction

The development of realistic surgical simulation systems requires accurate modelling of soft organs and their interactions with surgical instruments in typical surgical procedures such as needle insertion, incision and dissection. Phenomenological models rely on fitting various functions to experimentally obtained force-displacement relations are by far the most commonly used approach in surgical simulation. DiMaio and Salcudean [1, 2], Okamura and Simone [3] used phenomenological models to simulate needle insertion into very soft tissue and described needle forces as functions of insertion depth and relative velocity between needle and tissue. Its application made it possible to build interactive simulators with real-time kinaesthetic and visual feedback [2]. However, the results predicted by such models are valid only for the specific surgical instrument and boundary conditions of the organ used in the experiment from which the models were derived. This implies that their predictive power is very limited. Applying appropriate methods of computational solid mechanics to predict the forces and deformations during surgery eliminates this drawback. In practice, finite element method has been used for such predictions [4-7]. To account for the non-linear constitutive properties of soft tissue and large local deformation of soft organ occurs in surgical procedures [8-11], non-linear finite element procedures that take into account of both geometric (i.e., finite deformations) and constitutive non-linearities must be used.

For instance, non-linear finite element procedures implemented in the commercial finite element code LS-DYNA have been used by Wittek et al. to compute the instrument forces and soft tissue deformations during needle insertion and indentation into the swine brain [6]. However, the magnitude of force prediction was overestimated by approximately 25% in indentation and underestimated by approximately 30% in needle insertion. Wittek et al. provided only a very general discussion of possible sources of the discrepancies between the modelling and experimental results and did not conduct quantitative analysis of these sources. This can be attributed to the fact that when modelling such complex phenomenon as indentation or needle insertion in the actual brain, it is very difficult to distinguish between the inaccuracies due to finite element modelling by itself and uncertainties when experimentally determining the tissue properties and organ boundary conditions.

In this study, we evaluated the accuracy of non-linear finite element analysis in surgical simulation through its application in modelling of indentation of the human brain phantom. Replacing the actual brain with the phantom allowed us to conduct experiments under accurately controlled conditions and eliminate the uncertainties due to the lack of the quantitative data of the mechanical properties of the brain meninges and limited accuracy when determining the constitutive properties of soft tissues, that were suggested in the literature [7-12] as possible sources of inaccuracies when modelling surgical procedures.

The evaluation of the finite element model accuracy was done in terms of its ability to predict the forces acting on the surgical instrument (indenter) and the deformations due to these forces. Deformation field within the phantom was determined by tracking 3D motions of the X-ray opaque markers implanted in a pattern designed to sufficiently

cover the direct neighbourhood of indentation. To facilitate the construction of this marker pattern, the brain phantom was made layer by layer. To verify the experimental techniques including those for tracking marker motions, we also performed indentation experiment with the same setup on a multiple layers cylindrical specimen that was made using the same material and manufacturing techniques as the brain phantom.

As indicated in the study scheme shown in Fig. 1, the subsequent sections of this paper present the following topics: Section 2 describes the experiment setup and determining of the marker displacements. Section 3 deals with the non-linear finite element modelling of brain phantom indentation. Section 4 compares the experimental and modelling results. The discussion is included in section 5.
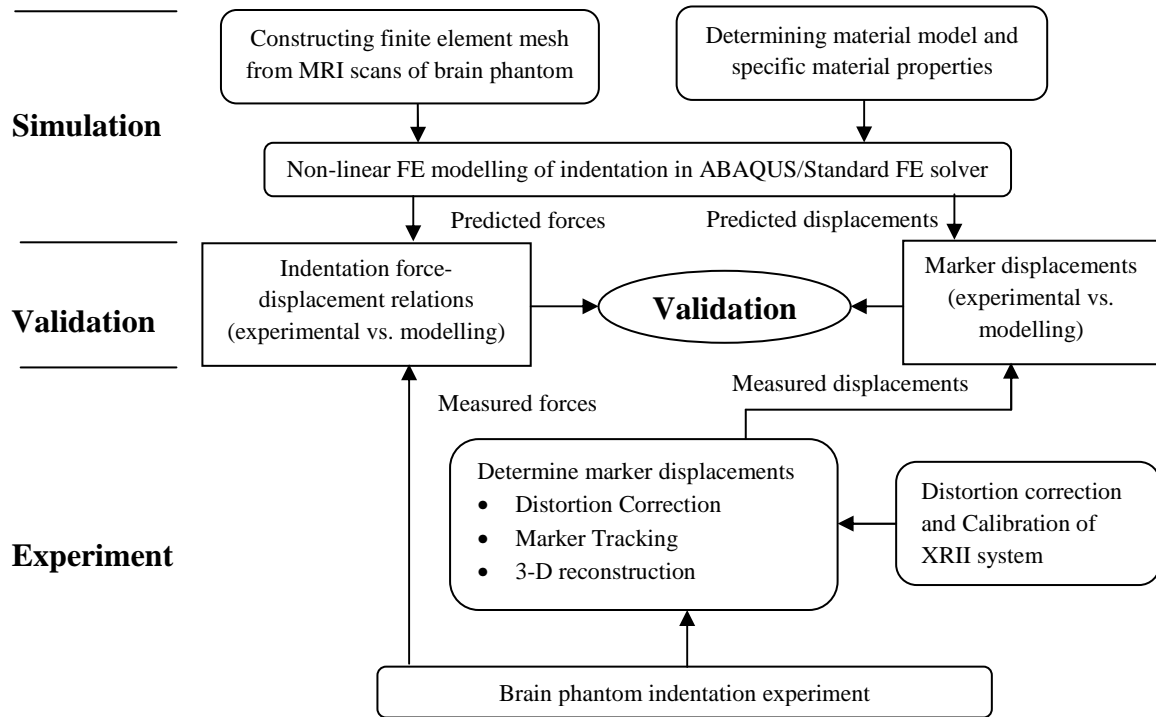
Simulation

| Constructing finite element mesh from MRI scans of brain phantom | Determining material model and specific material properties |

Non-linear FE modelling of indentation in ABAQUS/Standard FE solver

Predicted forces   Predicted displacements

Validation

| Indentation force-displacement relations (experimental vs. modelling) | **Validation** | Marker displacements (experimental vs. modelling) |

Measured forces   Measured displacements

Experiment

Determine marker displacements
- Distortion Correction
- Marker Tracking
- 3-D reconstruction

Distortion correction and Calibration of XRII system

Brain phantom indentation experiment

Fig. 1 Study Scheme

2. Experiment

2.1 Experiment preparation

2.1.1   Brain phantom preparation

The brain phantom was made of *Sylgard 527* dielectric silicone gel (Dow Corning Silicones Midland, MI, USA) which has been used [13, 14] to simulate the mechanical responses of the human brain tissue. The *Sylgard 527* gel was prepared by mixing two

components at the ratio of 1:1. X-ray opaque markers (steel beads with a diameter of 0.3 mm) were planted within the phantom to capture the deformation in the direct neighbourhood of indentation (the part of phantom directly under indenter). The beads were planted following a pattern designed to sufficiently cover the direct neighbourhood of indentation.

In the indentation experiment, the brain phantom was confined in a human skull cast (3B Scientific, Hamburg, Germany). In order to place the markers according to the designed pattern, the brain phantom was made layer by layer. For each layer, a small amount of the *Sylgard 527* gel was mixed, applied into the skull and kept in oven at 60 ℃ for 24 hours until the mixture reached non-flow state. Then the steel beads were placed on the gel surface according to the pattern design. This procedure was repeated until the marker pattern and brain phantom was fully constructed. Since only a small amount of gel was used for each layer, it was difficult to ensure that for every layer the two compounds were mixed exactly at the ratio of 1:1. Therefore, it was expected that different gel layers may exhibit different material properties. To facilitate determination of the specific material constants for layers, cylindrical samples (height of ~24 mm and diameter of ~30 mm) was made from the same batch of *Sylgard 527* gel used in the brain phantom layers. The samples were cured under the same conditions. A rectangular (80×40 mm) hole was opened on the top of skull cast to allow the indenter access to the brain phantom (Fig. 2).

2.1.2   Brain phantom preparation

Prior to the preparation of the brain phantom, the same manufacturing procedures were applied to make a multiple layers cylindrical specimen with identical pattern arrangement of markers. The multiple layers specimen was used to practice the layer-by-layer manufacturing procedures and to verify the experimental techniques including those for tracking marker motions.

2.2 Experimental setup

2.2.1   Brain phantom indentation setup

Indentations into brain phantom were performed using a custom-built apparatus consisting of a linear motion drive with a load cell and a stationary base as illustrated in Fig. 2. The human skull cast that contains the brain phantom was supported by a plaster base glued to the stationary platform. The indenter was attached to the load cell by a connecting shaft. Only the forces acting in the longitudinal direction of the indenter were measured and analysed because the indenter was much stiffer than the brain phantom and no indenter or shaft deflection was observed in the experiment.

As illustrated in Fig. 2, solid cylindrical aluminium indenter with a diameter of 10 mm and chamfer of 0.5×0.5 mm was used. The indentation speed was kept constant at 1 mm/s and the indentation depth (the indenter displacement measured from the start of contact between the indenter and brain phantom until the indenter reaches the farthest point of indentation) was approximately 9 mm. The displacement of the indenter was measured by a laser range scanner. The indentation forces and indenter displacement was acquired at the sampling rate of 30 Hz.

2.2.2   Multiple layers specimen indentation setup

Indentation into the multiple layers specimen was done by the same apparatus as used in brain phantom indentation experiment. The bottom surface of the multiple layers specimen was rigidly constrained by a sand sheet glued to the stationary platform (Fig. 2). The same solid aluminium indenter was used as in the case of brain phantom indentation. Following the setup of brain phantom indentation experiment, the indentation speed was kept constant at 1 mm/s. The indentation depth was approximately 10 mm.
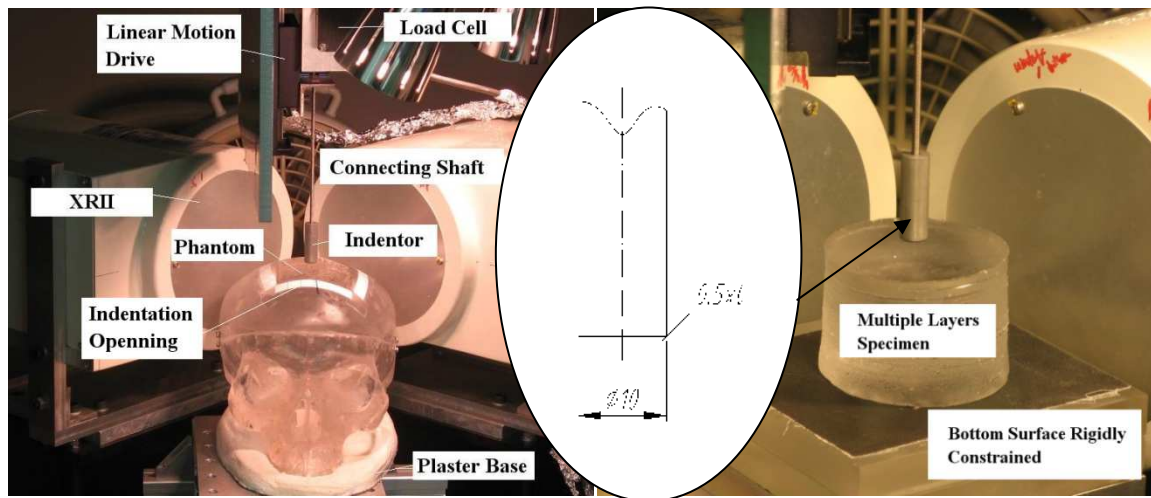

Fig. 2 Setup of brain phantom/multiple layers specimen indentation experiments and indenter geometry.

2.3 Determining the specific material constants

Miller and Chinzei [9-10] and Miller [11] used Ogden-type hyperviscoelastic material model to describe brain tissue constitutive behaviour. However, we found that the constitutive properties of the *Sylgard 527* gel used as substitution of brain tissue in this study do not exhibit significant strain-rate dependency. Therefore, the gel was modelled by Ogden-type hyperelastic material model described by the following formula [15].
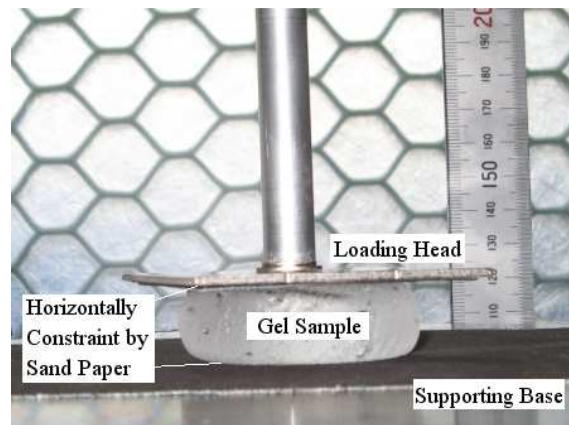
$$W = \frac{2\mu}{\alpha^2}(\lambda_1^\alpha + \lambda_2^\alpha + \lambda_3^\alpha - 3) \qquad\qquad 2.1$$

Where W is a potential function, λ_is are principle stretches, μ is the relaxed shear modulus, and α is a material coefficient which can assume any real value without any restriction. Although data regarding the relaxed shear modulus μ of *Sylgard 527* gel (see Eq. 2.1) have been reported in the literature [13, 14], data regarding the material coefficient α was not available. Moreover, we noticed that small difference in the mixing ratio of the two compounds of *Sylgard 527* gel could results in significant difference in the mechanical responses of the cured gel. Therefore, the cylindrical samples made along with the layers were tested by semi-confined uniaxial compression to determine the specific material constants. In the tests, the top and bottom surfaces of the samples were rigidly constrained in horizontal direction to the surfaces of the supporting base and loading head as shown in Fig. 3a and Fig. 3b. Nine loading cycles were executed on each sample at three different constant speeds of 10, 50 and 500 mm/min (0.167, 0.83 and 8.33 mm/s) to assess the repeatability of the experiment results and determine the strain-rate dependency of the gel constitutive properties. The average nominal stress-strain relations obtained at three different speeds on one gel sample are illustrated in Fig. 3c. From this figure, it is clear that *Sylgard 527* gel does not exhibit significant strain-rate dependency. When the loading speed was increased by 50 times, the relaxed shear modulus increased by less than 5%.

When determining the brain tissue constitutive properties using the compression tests of the brain tissue samples, Miller and Chinzei [9-10] and Miller [11] assumed orthogonality of the deformation state in the plane of sample symmetry. However, Morriss et al. [12] showed that when the samples were compressed more than 15% of its initial height, the assumption with about orthogonality of the deformation state no longer holds and suggested that finite element model of the compression tests should be used to determine the material constants of very soft tissue. Therefore, in this study the specific material constants of the gel samples were determined by calibrating the models of the uniaxial compression tests of the silicone gel samples implemented using ABAQUS finite element solver. The typical average force-displacement relations obtained from experiment and the corresponding modelling results are shown in Fig. 3d.
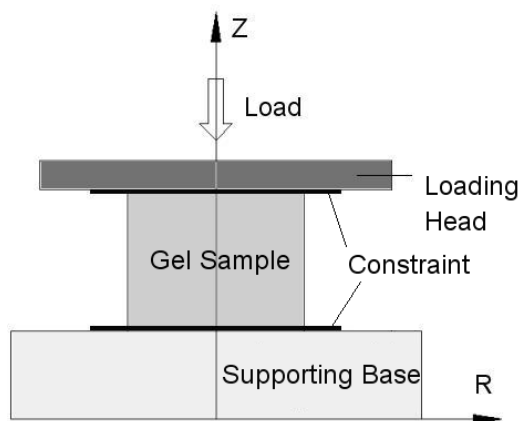
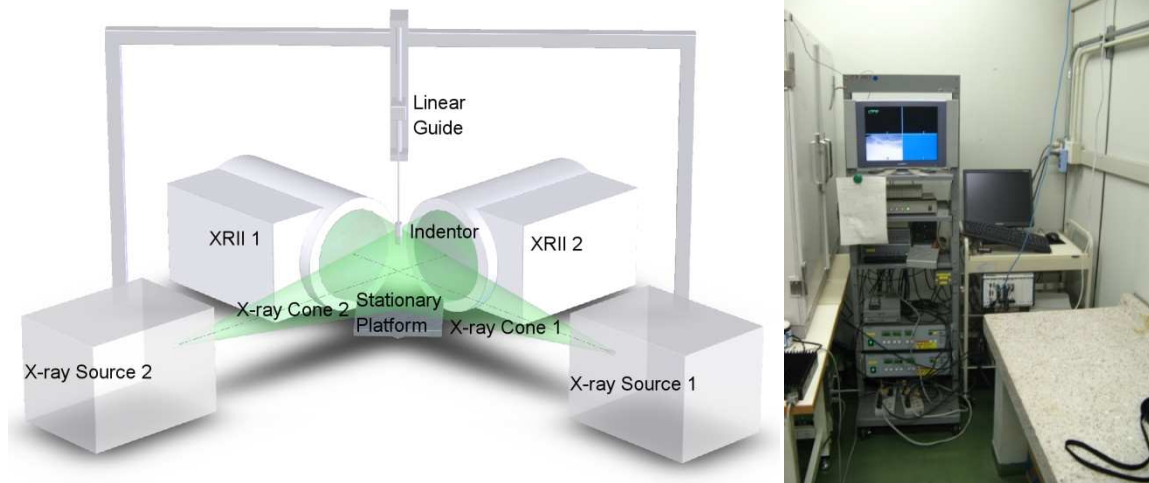(a) Compression test setup.   (b) Photograph of compression test.
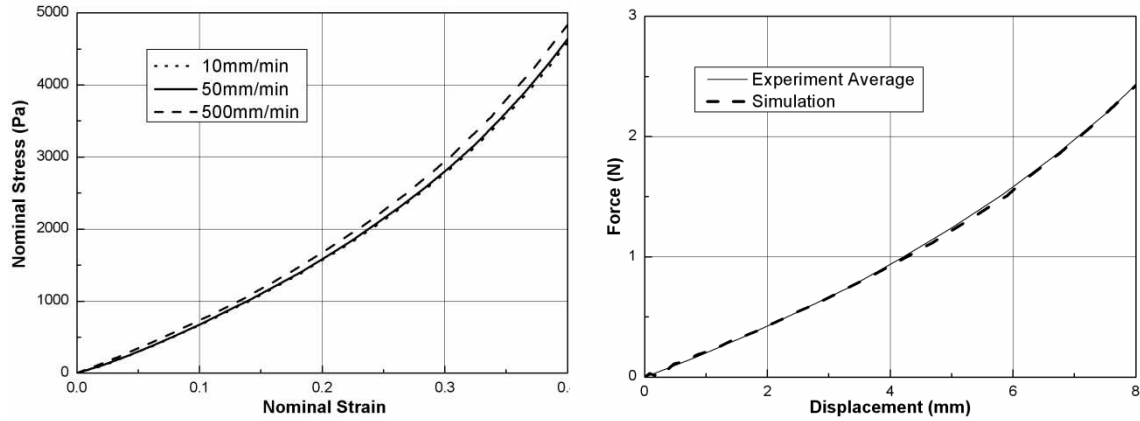
(c) Average experimental nominal stress-strain relationship at three loading speeds.

(d) Experimental and modelling force-displacement relations at the loading speed of 500 mm/min.

Fig. 3 Compression test to determine the material constants.

(a) Setup of the bi-plane XRII system.   (b) Image acquisition unit

Fig. 4 Custom-made bi-plane XRII system.

2.4 Determining marker displacements

Fig. 4 shows the custom-made bi-plane X-ray Image intensifiers (XRII) system (Surgical Assist Technology Group, AIST, Tsukuba, Japan) used to track the motions of the X-ray opaque markers planted within the multiple layers specimen and brain phantom. It consists of two sets of X-ray sources and X-ray image intensifiers (E5881J-P1) produced by Toshiba Electron Tubes & Devices CO., LTD and an imaging acquisition

unit made by National Instrument. These XRIIs provides high resolution (77LP/cm) and contrast (22:1) for tracking the markers. The two XRIIs were positioned so that their imaging planes were orthogonal to each other, allowing synchronized bi-plane real time imaging of the markers and indenter during indentations. The videos were captured by the image acquisition unit at 30 frames per second and a resolution of 640×480 pixels.

2.4.1   Distortion correction and calibration

To accurately extract the positions of the markers in the recorded X-ray images, the geometrical distortions of the image need to be removed. In an XRII, there are mainly two types of distortions: pincushion distortion (positive radial distortion) caused by projecting a flat surface onto a global surface (the input sulphur screen of the XRII) and spiral distortion caused by the deflection of electrons due to earth's magnetic field [16-17]. The CCD camera used to capture the intensified light image also induces radial distortion and tangential distortion due to imperfection of the lens elements [18-20]. In our experiments, the effect of spiral distortion was found negligible. Therefore, only radial and tangential distortions were considered. By combining these distortion components, the total distortion $[\delta_x, \delta_y]^T$ at an image point $Q(x, y)$ in terms of camera reference frame (CRF) can be summarized in the following expression [21-23].

$$\begin{bmatrix} \delta_x \\ \delta_y \end{bmatrix} = \begin{pmatrix} k_1 xr^2 + k_2 xr^4 \\ k_1 yr^2 + k_2 yr^4 \end{pmatrix} + \begin{bmatrix} 2t_1 xy + t_2(r^2 + 2x^2) \\ t_1(r^2 + 2y^2) + 2t_2 xy \end{bmatrix} \qquad 2.2$$

Where (u', v') is the coordinate of point Q with respect to the principle point (centroid) of the image plane; $r = \sqrt{u'^2 + v'^2}$ is the distance from the point Q to the principle point, k_1, k_2 are the coefficients of radial distortion, and t_1, t_2 are the coefficients of tangential distortion.

To reconstruct 3D displacements of the implanted markers, the camera parameters need to be estimated through calibration. Following Hing et al. [5], Navab et al. [21] and Mischke et al. [22], the projection geometry of an XRII was approximated by a pinhole camera model illustrated in Fig. 5. It can be described as a transformation from the 2D homogeneous coordinates $u = [u, v, 1]^T$ in the image reference frame (IRF) to 3D homogeneous coordinates $X = [X, Y, Z, 1]^T$ in the world reference frame (WRF)

$$u = \mathbf{P} \cdot X, \qquad\qquad\qquad 2.3$$

where **P** is the projection matrix that contains the camera parameters. These parameters can be divided into two sets: (1) The intrinsic parameters **A** described by the 3×4 matrix define the transformation between IRF and CRF; (2) The extrinsic parameters **T** described by 4×4 homogeneous transformation matrix define the position (**t**) and orientation (**R**) of CRF in the WRF [23-24]. Using the intrinsic and extrinsic parameters, the camera projection matrix can be expressed as

$$P = A \cdot T = \begin{bmatrix} \alpha_u & 0 & u_0 & 0 \\ 0 & \alpha_v & v_0 & 0 \\ 0 & 0 & 1 & 0 \end{bmatrix} \cdot \begin{bmatrix} R & t \\ 0^T & 1 \end{bmatrix},$$ *2.4*

where $(\alpha_u, \alpha_v)^T$ presents the equivalent focal length in terms of pixel dimensions in u and v direction respectively, $(u_0, v_0)^T$ is the coordinate of the principle point of the image plane in pixels.
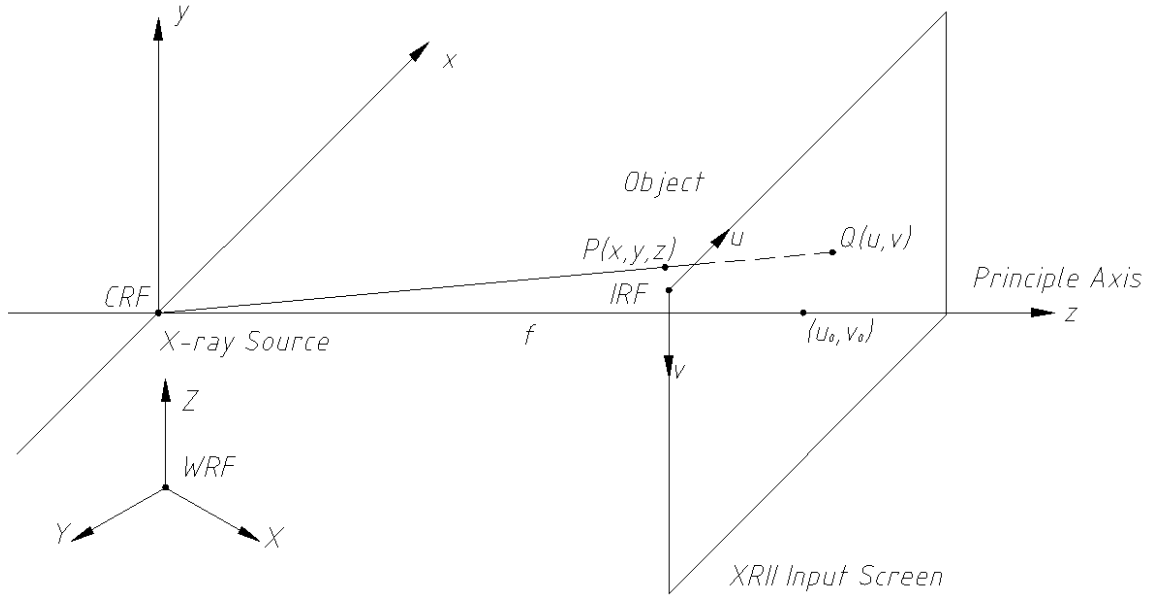

Fig. 5 The projection geometry of a distortion free XRII can be approximated as a pinhole camera model.
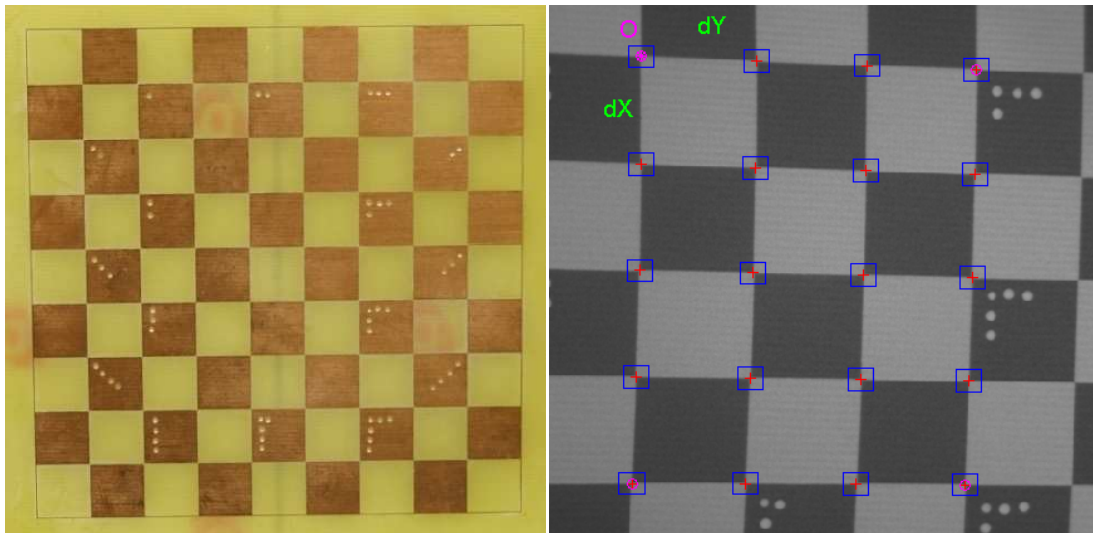

Fig. 6 The chessboard calibration grid planar pattern used in this study. The dimension of the blocks is 10×10 mm, the intersections were used as control points for distortion correction and calibration.

The camera calibration method proposed by Zhang [25-26] was used to determine the camera parameters and distortion coefficients. It requires the camera to observe a planar pattern shown at several different orientations. We used a chessboard pattern made by eroding copper from a Printed Circuit Board (PCB) as illustrated in Fig. 6. The camera parameters and distortion coefficients were computed using the Camera Calibration Toolbox for Matlab developed by Bouguet [27] in which radial and tangential distortions are modelled. The estimated camera parameters and distortion coefficients are listed in Table 1. The average, maximum and standard deviation of re-projection error indicate the accuracy of determining the 3D position of an object point from the X-ray images is provided in Table 2.

Table 1. Estimated distortion coefficients and camera parameters

XRII Parameters	Distortion Coefficients				Camera Parameters (pixel)			
	k_1	k_2	t_1	t_2	α_u	α_v	u_0	v_0
Left	3.05	-245.47	-0.019	-0.066	4288.16	4284.61	239.5	319.5
Right	3.00	-194.69	-0.040	0.071	4544.46	4471.93	246.5	313.5

Table 2. Estimated re-projection errors

Re-projection Error	In pixel			In millimetres		
	Average error	Standard deviation	Maximum error	Average error	Standard deviation	Maximum error
Left	0.6971	0.3199	2.1193	0.077	0.035	0.233
Right	0.3075	0.1733	1.1478	0.034	0.019	0.126

2.4.2   Marker tracking and 3-D reconstruction

The X-ray opaque markers were tracked using an in-house code implemented in MATLAB. Zilla Video Converter Decompiler (Zilla Softwares) was used to decompile the videos into image sequences in Tagged Image File (TIF) format. The geometrical distortions were removed according to the estimated distortion coefficients using the Camera Calibration Toolbox for Matlab [27]. The centroids of the markers were extracted from the X-ray images using phase congruency corner detector developed by Kovesi [28-30]. We incorporated the distortion correction and corner detection functions into our tracking code. Between every two consecutive frames we only look at the neighbourhood of a particular marker to locate and update the position of that marker. In this way, the computation efficiency was significantly improved.

The tracking code determines the positions of the markers up to a sub-pixel level by fitting a parabola to the neighbourhood of the marker. To determined the uncertainty of the results obtained using our tracking code, we applying it to determine the marker positions in 50 image frames recorded when no load was applied to the brain phantom so the markers were stationary. The maximum standard deviation of determining marker positions in such circumstance is determined to be 0.00167 pixels. Therefore the uncertainty induced by our tracking code is negligible comparing to the uncertainty due

to the distortion correction and calibration. We used the triangulation functions in the Camera Calibration Toolbox for Matlab [27] to compute 3D positions of the markers. According to the estimated re-projection errors listed in Table 2, the maximum error could occur in determining the marker position is 0.359 mm.

# 3. Modelling

3.1 Finite element mesh

3.1.1   Brain phantom mesh

The geometry of the brain phantom was obtained from the magnetic resonance images (MRI) in which the brain phantom was rigidly constrained by the human skull cast and plaster base so it accurately represents the geometry of the brain phantom during indentation experiment. A digital model of the brain phantom surfaces was constructed from MRI scans using 3D SLICE 3.0 software package (http://www.slicer.org) and exported in a Visualization Toolkit (VTK) binary format [31]. Then it was converted by an in-house code into a Hypermesh compatible finite element input file and imported into Hypermesh finite element mesh generator (Altair Engineering, Troy, Michigan, USA). The Hypermesh geometry builder module was used to patch and merge the imported surfaces into a closed surface defining the entire brain phantom surface. This closed surface was used as the boundary when conducting volumetric discretization using an automatic mesh generator (Hypermesh) with second order tetrahedron elements (type C3D10H in ABAQUS, 10-node quadratic tetrahedron) [32]. As the *Sylgard 527* gel used to substitute brain tissue is virtually incompressible, second order elements with mixed formulation and constant pressure were selected to prevent volumetric locking [33]. As illustrated in Fig. 7a, the resulted brain phantom mesh consists of 41570 nodes and 27716 elements.

The characteristic length of the brain phantom mesh was approximately 5 mm. In order to accurately model the indenter-brain phantom interactions, in the indentation area (cylindrical of diameter of ~22mm and height of ~10mm) the mesh was refined to the characteristic length of 3 mm (Fig. 7b). As shown in Fig. 7, to model the multiple layers structure of brain phantom, the brain phantom mesh was divided into 4 element sets according to the dimensions of the layers.

As the solid cylindrical indenter (diameter of 10 mm with chamfer of 0.5×0.5 mm) made of aluminium was orders of magnitude stiffer than the brain phantom, it was modelled as a rigid body. Consequently, only the surface of the indenter had to be included in the

model to define the contact with the brain phantom. The indenter surface was discretized by 3-node and 4-node shell elements.
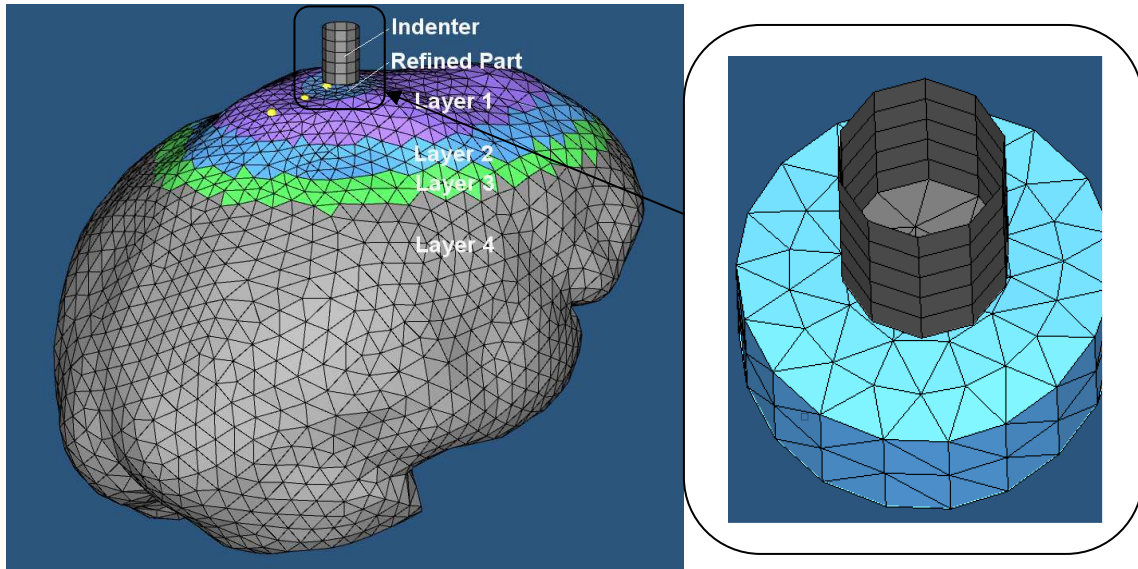
(a) General view of the brain phantom mesh used in this study   (b) Refined mesh part and indenter.
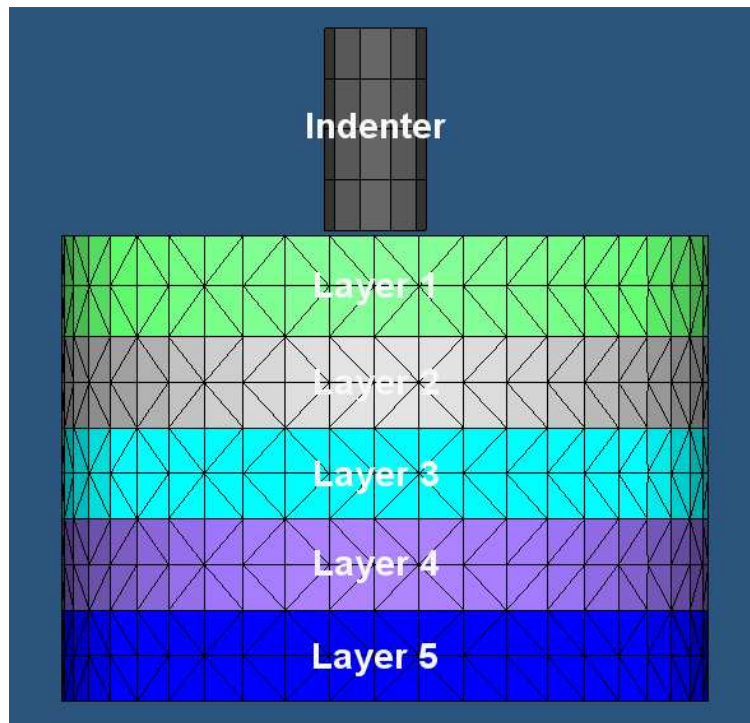
Fig. 8 Brain phantom mesh.

Fig. 9 Multiple layers specimen mesh.

3.1.2   Multiple layer specimen mesh

Initially, we modelled indentation on the multiple layers specimen to verify the non-linear finite element procedures used in the model of brain phantom indentation. The outer surface defining the geometry of the multiple layers specimen was generated by the Hypermesh geometry builder module according to the measured dimensions (height of 46 mm, diameter of 64 mm, and layer thickness of 9 mm). The volume taken by each layer was discretized by the Hypermesh automatic mesh generator with the same type of second order tetrahedron elements used in the brain phantom mesh. As illustrated in Fig. 8, the resulted multiple layers specimen mesh consists of 13995 nodes and 9195 elements. The characteristic length was approximately 3 mm. The indenter surface was discretized by 3-node and 4-node shell elements.

3.2 Contact formulations, loading, and boundary conditions

3.2.1   Contact formulations and loading

The indentation was modelled as contact interactions between a rigid body (the indenter) and a deformable surface (brain phantom or multiple layers specimen mesh). To account for the change of direction of the indenter surface normal, the contact interaction was modelled as two contact pairs: (1) the contact between head surface of the indenter and the deformable surface of the brain phantom (Fig. 9a), (2) the contact between the side surface of the indenter and the deformable surface of the brain phantom (Fig. 9b). Both of them were modelled using surface-to-surface penalty contact formulations with augmented Lagrange constraint enforcement. When conducting the experiments, we noticed that the silicone gel sticks firmly to the indenter, therefore rough friction (no slip once points are in contact) conditions of ABAQUS were used for the contact pairs.
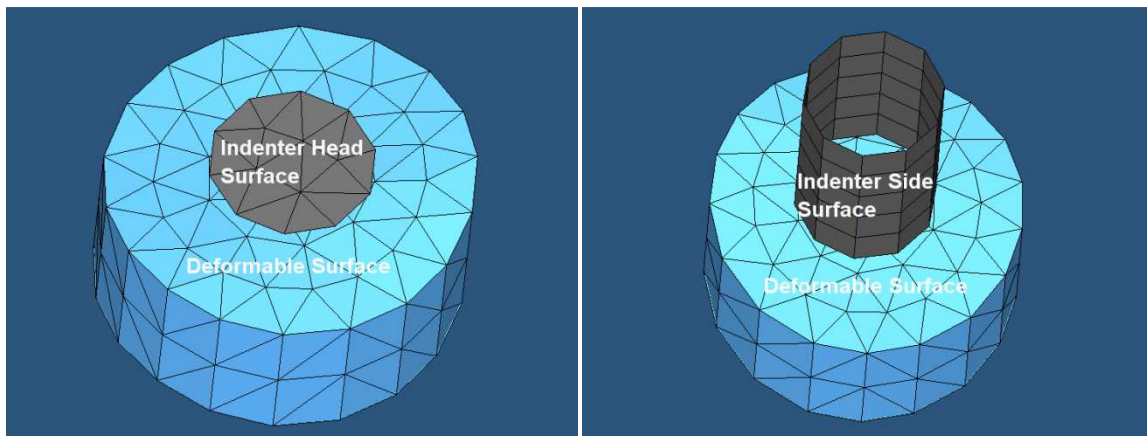
(a) Pair 1: Head surface of the indenter and deformable surface of the brain phantom

(b) Pair 2: Side surface of the indenter and deformable surface of the brain phantom.

Fig. 9 The two contact pairs.

The model was loaded by motion of the indenter. The loading was prescribed at the constant speed of 1 mm/s for 9 seconds which was corresponding to the indentation depth of approximately 9 mm.

3.2.2   Boundary condition for brain phantom indentation

The human skull cast that contains the brain phantom was constraint by the plaster base which was rigidly glued to the stationary platform in the indentation experiment (Fig. 2). We noticed that the brain phantom sticks firmly to the human skull cast. Therefore the nodes defining the brain phantom surface except the rectangular hole opened for the indenter to access the brain phantom were rigidly constrained in the model (Fig. 10a).

3.2.3   Boundary condition for the multiple layers specimen

In the experiment, the bottom surface of the multiple layers specimen was rigidly constrained by a sand sheet glued to the stationary platform (Fig. 2). Therefore nodes defining this surface were rigidly constrained in the model (Fig. 10b).
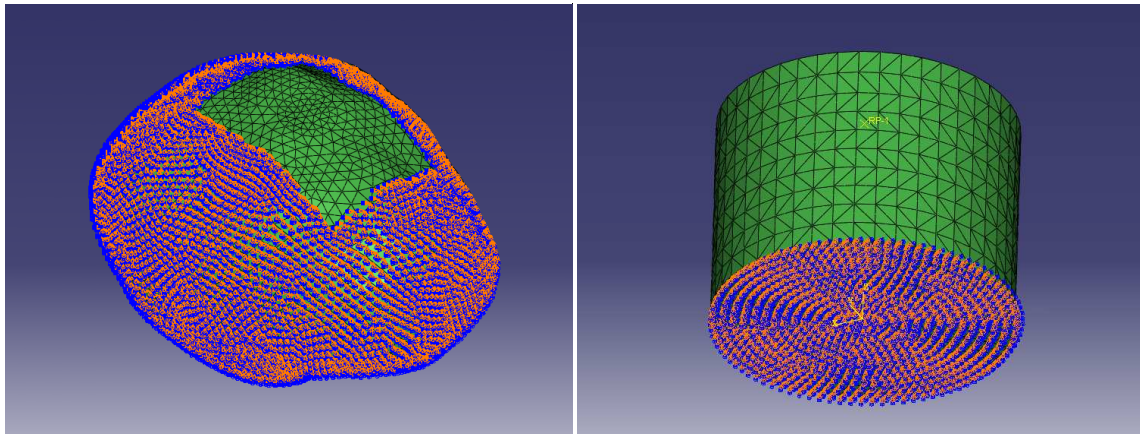
(a) Boundary condition for brain phantom indentation model.

(b) Boundary condition for multiple layers specimen indentation model.

Fig. 10 Boundary conditions in the finite element model

4. Results

4.1 Brain phantom indentation

For Ogden type hyperelastic material constants (eq. 2.1) shown in table 3, the finite element model shown in Fig. 8 accurately predicted the indentation force-displacement relations (Fig. 11) and marker displacements (Fig. 12). For indentation depth up to 9.4 mm, the discrepancy of indentation force magnitude is less than 5%. The displacements of the markers were computed from the nodal displacements predicted by the model

through quadratic shape functions of the second order tetrahedron elements [34, 35]. The comparison between the marker displacements predicted by our model with the actual marker displacements determined from the experiment at the indentation depth of 9.4 mm is shown in Fig. 12a. The comparisons between the initial positions of the markers with the modelling and experimental final positions of the markers at the same indentation depth are shown in XY, YZ, and XZ planes (Fig. 12b, Fig.12c and, Fig.12d). The maximum, minimum and average of the x, y, z components and magnitude of the discrepancies between the model prediction and actual marker displacements are shown in Table 4. The average error in magnitude is 0.3186 mm, which is within the accuracy of determining the actual marker displacements from the X-ray images. Additional evidence indicates good agreement between the modelling and experimental deformation is that the some markers in the edge of the pattern were found moving upwards in the experimental results and our model actually predicted this trend (Fig 12a).

The likely reasons for the discrepancies between experimental and modelling results are the approximations of the marker pattern geometry and uncertainty when determining the location of the indention area on the brain phantom. In this study, the markers were manually placed by a tweezers with the reference to a template. The accuracy of placing the markers and accuracy of determining the location of the indentation area on the brain phantom is estimated to be no better than 1mm.
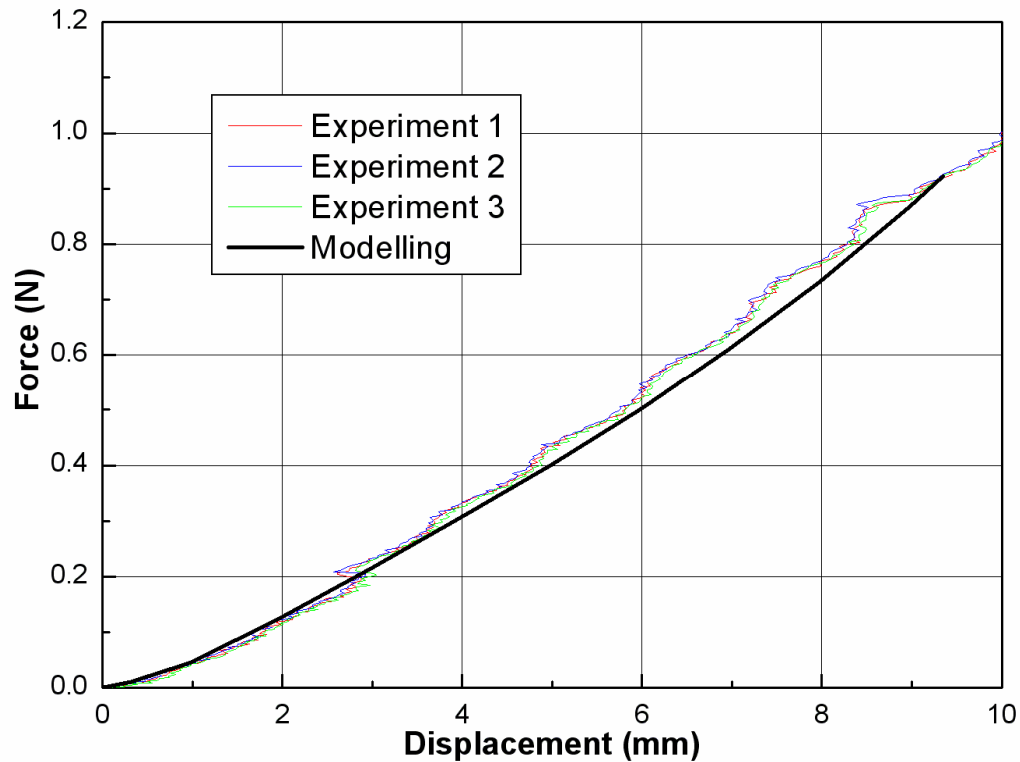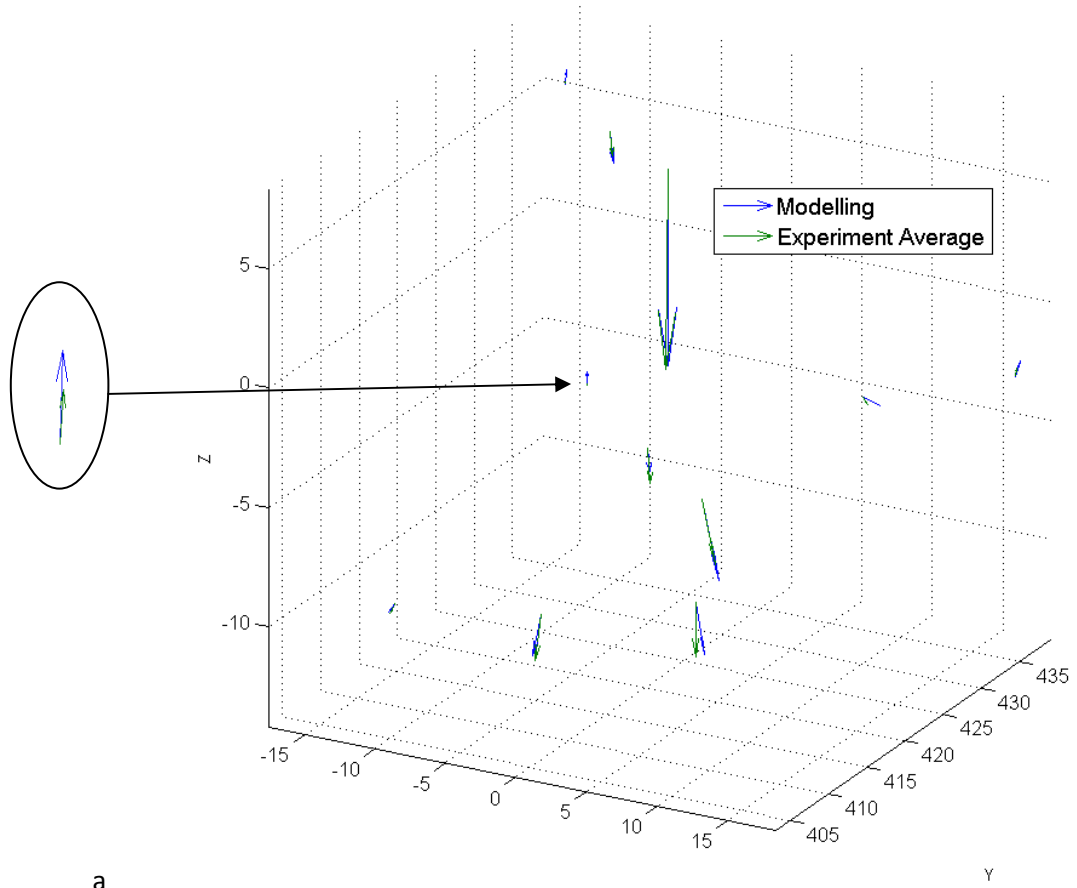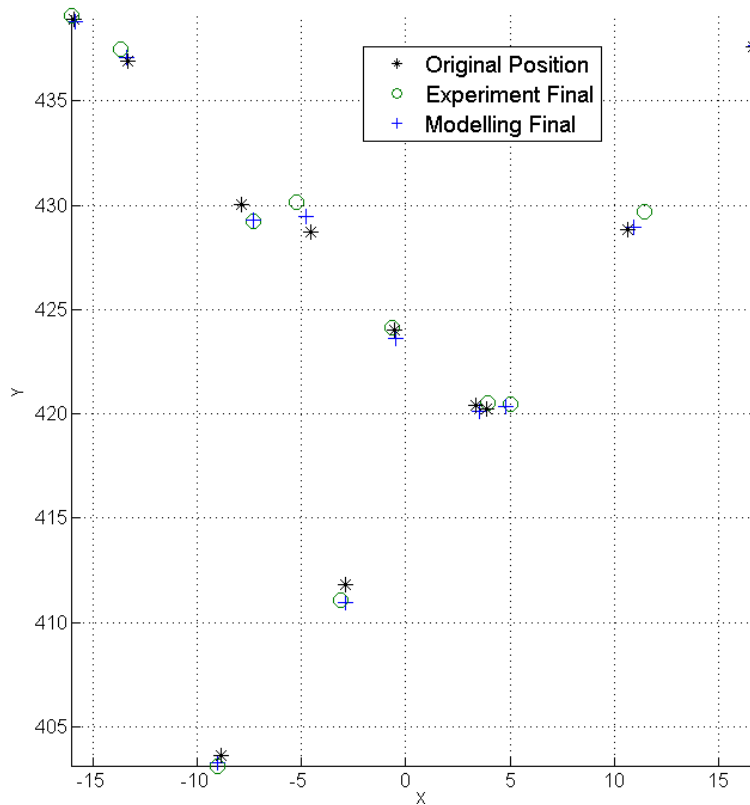

Fig. 11 Brain Phantom indentation: comparison of modelling and experimental results in force magnitude. The modelling results were obtained with Ogden type hyperelastic material constants listed in table 6 by ABAQUS/Standard.
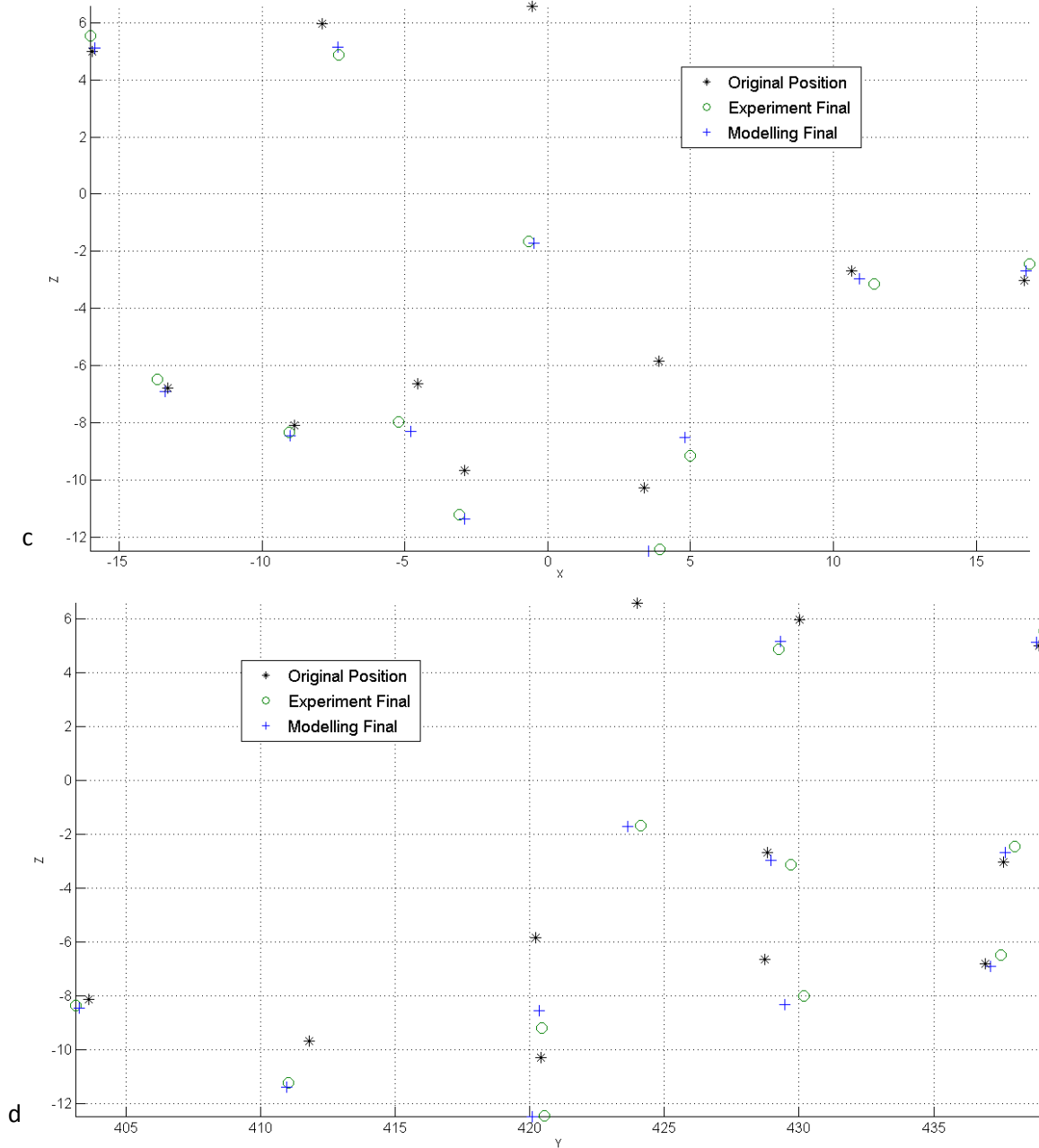
a

b

Fig. 12 Brain phantom indentation: (a) Comparison of the predicted and actual marker displacements at the indentation depth of 9.4 mm. The experimental results show that some markers at edge of the pattern actually moved upwards in the indentation. Our model accurately predicted this trend. (b), (c), (d) Comparisons of the initial positions with the modelling and experimental final positions of the markers at the indentation depth of 9.4 mm in XY, XZ, and YZ planes. The modelling results were computed through quadratic shape functions of the second order tetrahedron elements.

Table 4 Material constants for the layers of the brain phantom.

Layer	µ(Pa)	α
1	1875	4.9
2	1325	4.1
3	2300	3
4	3000	5

Table 5 The differences between the estimated and measured marker positions of brain phantom indentation.

Unit: mm	Maximum	Minimum	Average
x	0.5154	0.0285	0.2009
y	0.7219	0.0380	0.2897
z	0.6423	0.0216	0.2193
magnitude	0.8312	0.0002	0.3186

4.2 Multiple layers specimen indentation:

For the Ogden type Hyperelastic material constants of the multiple layers specimen listed in table 5, the finite element model shown in Fig. 9 accurately predicted the indenter force-displacement relations (Fig. 13) and marker displacements in multiple layers specimen indentation (Fig 14). The discrepancy of force magnitude between the experimental and modelling results was less than 5%. The marker displacements were computed in the same way as in brain phantom indentation. The comparison between the marker displacements predicted by the model and the marker displacements extracted from the X-ray images at the indentation depth of 10 mm is shown in Fig. 13a. The comparisons between the initial positions of the markers with the modelling and experimental final positions of the markers at the indentation depth of 10 mm are shown in XY, YZ, and XZ planes (Fig. 13b, Fig.13c and, Fig.13d). The maximum, minimum and average of the x, y, z, components and magnitude of the discrepancies between the predicted and actual marker displacements are shown in Table 6. The average error in magnitude is determined to be 0.4652 mm, which should be regarded as a very small error considering that the uncertainty of determining the actual marker displacements from the X-ray images is up to 0.359 mm.

In the multiple layers specimen indentation, in addition to the likely reasons for the discrepancies between experimental and modelling results described in the case of brain phantom indentation, another possible source of error is the approximations of the multiple layers specimen geometry. In this study, the multiple layers specimen geometry and the thickness of the gel layers were measured using a vernier caliper. As the Sylgard 527 gel is very soft (as it very closely represents the brain tissue mechanical properties), we estimate that accuracy of this measurement is not better than 1 mm.

Table 3 Material constants for the layers of the multiple layers specimen.

Layer	μ(Pa)	α
1	2200	4.2
2	2750	5.1
3	2225	5.1
4	2750	5.1
5	2300	3

Table 4 The differences between the estimated and measured marker displacements in multiple layers specimen indentation.

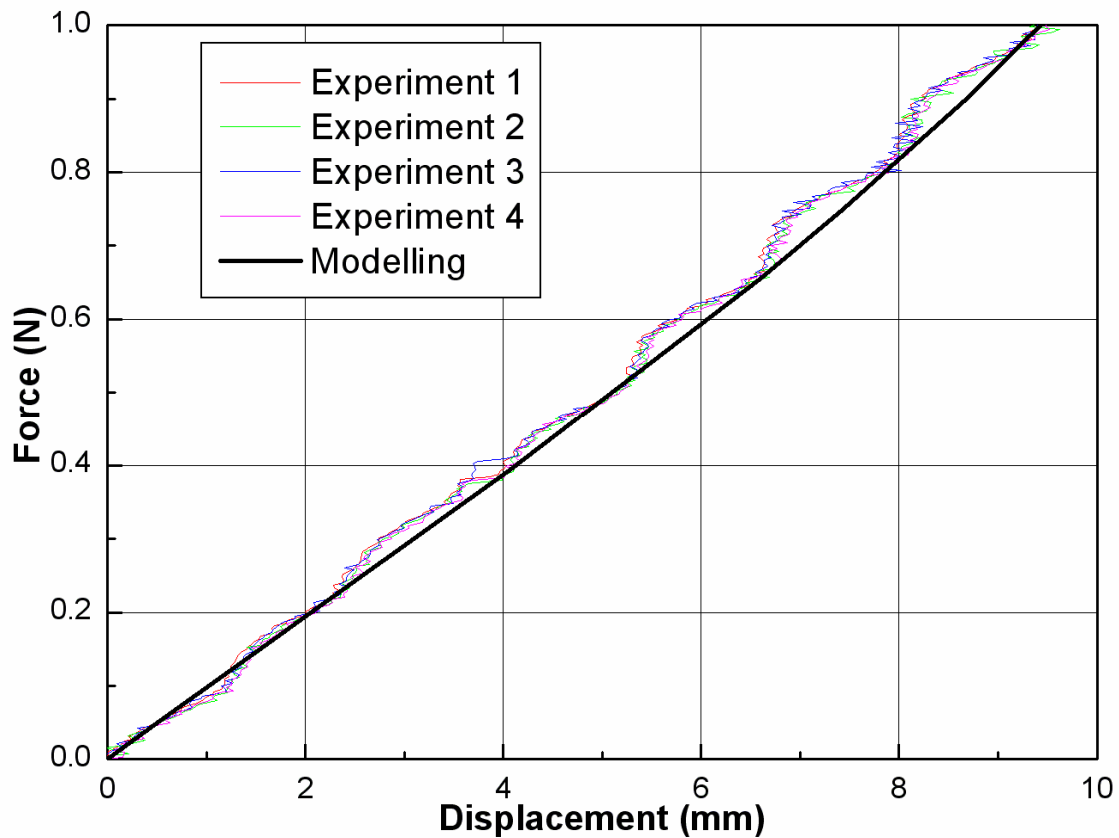| Unit: mm	Maximum	Minimum	Average
x	0.1565	0.0105	0.0755
y	0.5188	0.0276	0.2441
z	0.9613	0.2298	0.4840
magnitude	0.8364	0.0572	0.4652

Fig. 13 Multiple layers specimen indentation: comparison of modelling and experimental results in force magnitude. The modelling results were obtained with Ogden type hyperelastic material constants listed in table 3 by ABAQUS/Standard.

a

b
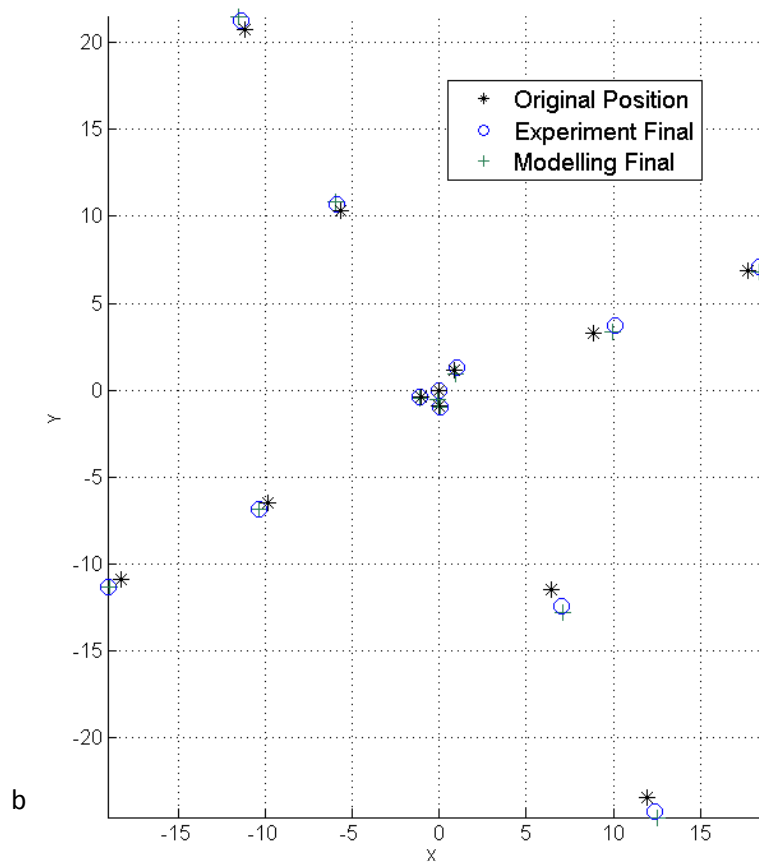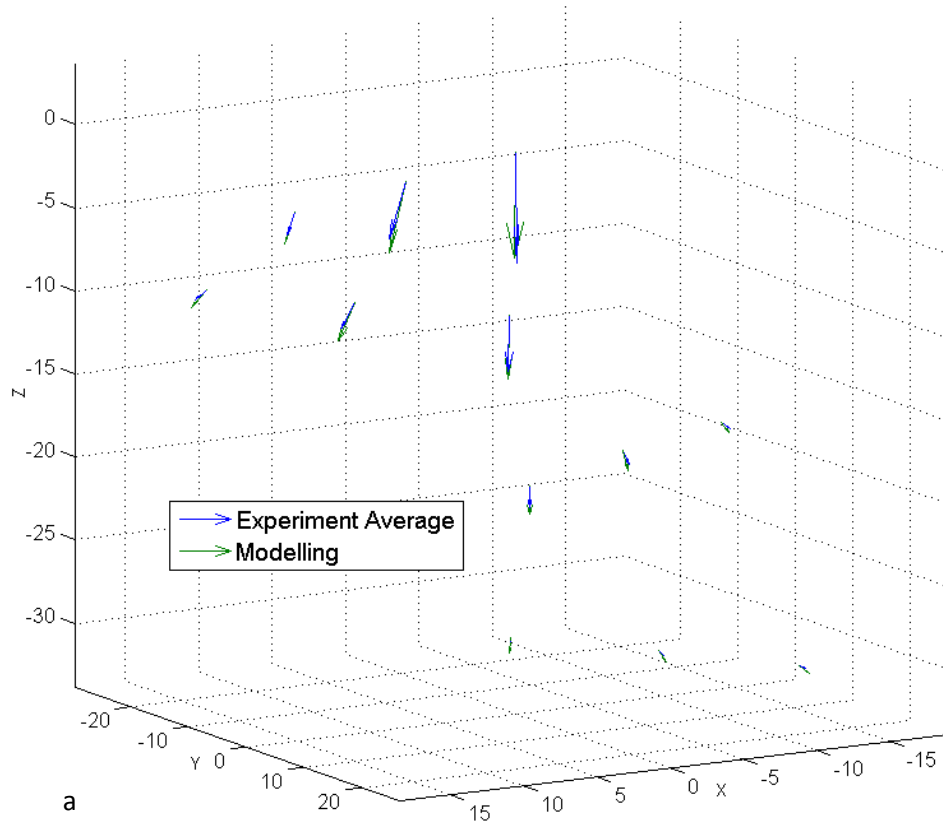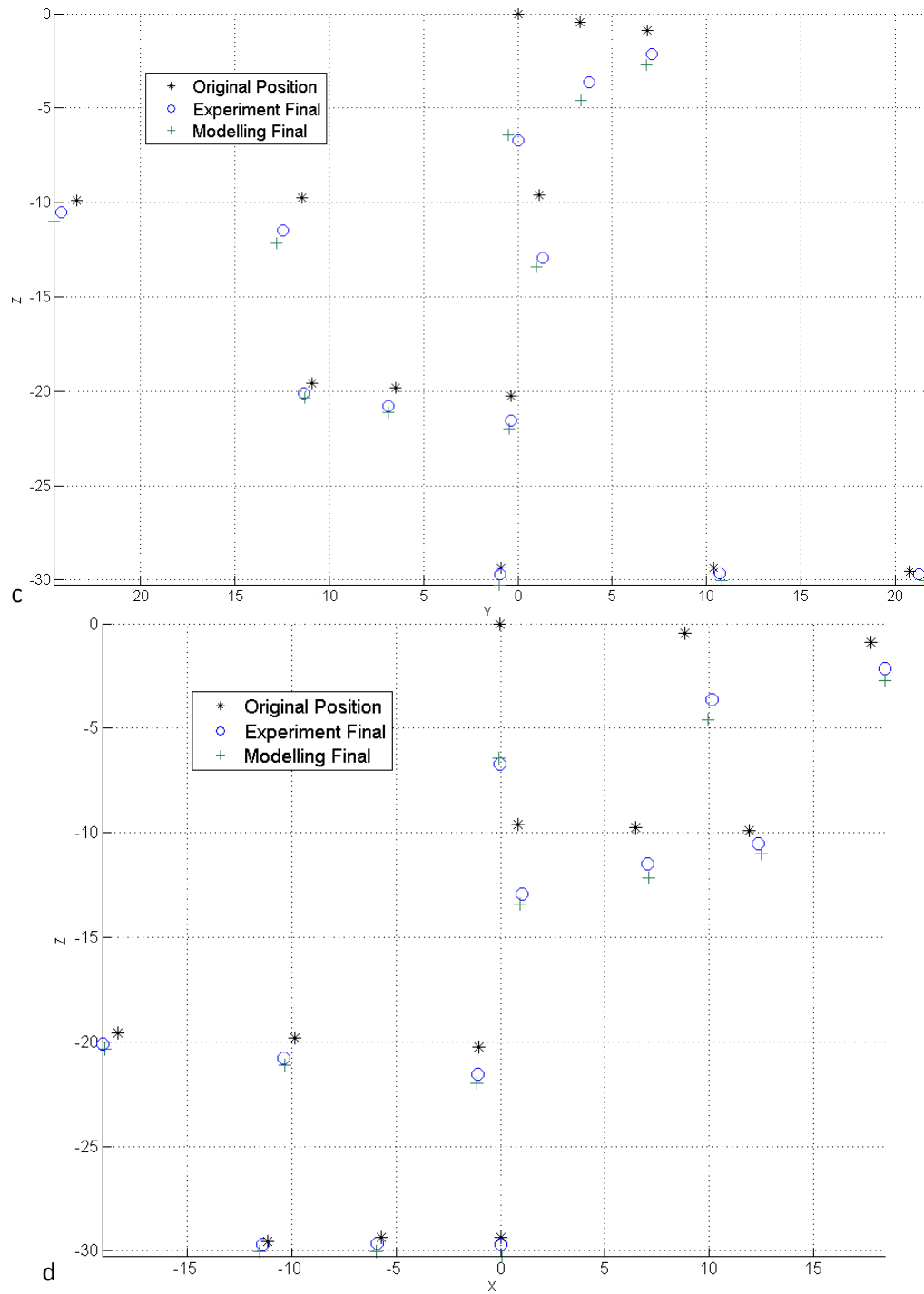
Fig. 14 Multiple layers specimen indentation: (a) Comparison of the predicted and measured marker displacements at the indentation depth of 10 mm. (b), (c) (d) Comparisons of the initial positions with the modelling and experimental final positions of the markers at the indentation depth of 10 mm in XY, XZ, and YZ planes. The modelling results were computed through quadratic shape functions of the second order tetrahedron elements by an in-house code.

5. Discussion

In this paper, we evaluated the accuracy of non-linear finite element analysis in surgical simulation through its application in modelling of indentation of the human brain phantom. To distinguish between the inaccuracies due to finite element procedures itself with inaccuracies due to simplifications in representing the boundary conditions and constitutive behaviour of soft tissue, we performed indentation experiments on the human brain phantom under accurately controlled experimental conditions. To capture the deformations of the brain phantom, we utilized image processing techniques to extract the displacements of the X-ray opaque markers placed in the direct neighbourhood of indentation from real time X-ray image sequences. To account for geometric and material non-linearities, we used non-linear finite element procedures with implicit time integration methods and Ogden type Hyperelastic material model for the brain phantom. The brain phantom was made layer by layer and the specific material constants were determined by compressing cylindrical samples made from the same batch of gel used in the layer. The indentation was modelled as contact interactions between a rigid body (the indenter) and a deformable surface (brain phantom). The experimental and modelling techniques were firstly verified by indenting a cylindrical multiple layers specimen with an identical marker pattern. For both multiple layers specimen indentation and brain phantom indentation, the finite element models accurately predicted the indentation forces (Fig.12, Fig. 14) and marker displacements (Fig.13, Fig. 15).

The modelling results presented in section 4 demonstrates that for accurately controlled experimental conditions and actual material constants data, non-linear finite element models can accurately predict the interactions between the surgical instrument (indentor) and soft organ (simulated with brain phantom) in terms of both instrument forces and soft organ deformations despite the complexity of the phenomenon. Good agreement between the modelling and experimental results also highlights the predictive power of the non-linear finite element modelling techniques used in this study. With notable exception of Wittek et al. [6], the previous studies [1-3] typically used phenomenological models that rely on fitting various functions to experimentally determined force-displacement relations to determine the forces acting on the surgical instruments. They do not predict but rather describe the soft organ responses. On the other hand, the modelling results presented in this study are results of prediction rather than fitting the model to experimental data. The indentation forces are computed directly from equations of continuum mechanics. The marker displacements are computed from the nodal displacements predicted by the model. The only experimental data required in our model is the specific material constants of the organ (simulated by the brain phantom) that can be determined by well established constitutive law and testing protocols [9-12].

One significant difference that separates our brain phantom indentation from real surgical procedures is the boundary conditions. The brain phantom was made of *Sylgard 527* gel that sticks firmly to the human skull cast, therefore clearly defined boundary conditions (rigid constraints) could be used in the model. However, the interactions between the brain tissue and brain meninges as well as the interactions between the brain and skull have not been thoroughly investigated. Further study towards understanding of the interaction mechanism of the brain tissue, brain meninges, and skull is required.

References

1. DiMaio, S. P. and Salcudean, S. E., 2003. Needle Insertion Modelling and Simulation. IEEE Transactions on Robotics and Automation 19(5): 864-874.
2. DiMaio, S. P. and Salcudean, S. E., 2005. Needle steering and motion planning in soft tissues. IEEE Transactions on Biomedical Engineering 52 (6): 965-974.
3. Okamura, A. M., Simone, C., et al. 2004. Force Modelling for Needle Insertion into Soft Tissue. IEEE Transactions on Biomechanical Engineering 51: 1707-1716.
4. Alterovitz, R., K. Goldberg, et al., 2003. Needle insertion and radioactive seed implantation in human tissues: simulation and sensitivity analysis. Paper presented at the IEEE International Conference on Robotics and Automation, Taipei, 1793-1799.
5. Hing, J. T., Brooks, A. D., et al. 2007. A biplanar fluoroscopic approach for the measurement, modelling, and simulation of needle and soft-tissue interaction. Medical Image Analysis 11(1): 62-78.
6. Wittek, A., Dutta-Roy, T., Taylor, Z., Horton, A., Washio, T., Chinzei K. and Miller K., 2007 Subject-specific non-linear biomechanical model of needle insertion into the brain. Computer Methods in Biomechanics and Biomedical Engineering, 11(2): 135-146.
7. Jordan, P. S., Socrate, et al., 2009. Constitutive modelling of porcine liver in indentation using 3D ultrasound imaging. Journal of the Mechanical Behaviour of Biomedical Materials 2(2): 192-201.
8. Fung, Y. C., 1993. Biomechanics: Mechanical Properties of Living Tissue. New York, Springer.
9. Miller, K. and Chinzei, K., 1997. Constitutive Modelling of Brain Tissue: Experiment and Theory. Journal of Biomechanics 30: 1115-1121.
10. Miller, K. and Chinzei, K., 2002. Mechanical Properties of Brain Tissue in Extension. Journal of Biomechanics 35: 483-490.
11. Miller, K., 2005. Method of Testing Very Soft Biological Tissues in Compression. Journal of Biomechanics 38: 153-158.
12. Morriss, L., Wittek, A., et al. 2008. Compression testing of very soft biological tissues using semi-confined configuration-A word of caution. Journal of Biomechanics 41(1): 235 - 238.
13. Brands, D.W.A., et al., 1999. Comparison of the dynamic behaviour of brain tissue and two model materials. In: Proceedings of the 43th Stapp Car Crash Conference: 57–64.
14. Brands, D.W.A., et al., 2000. The large strain dynamic behaviour of in-vitro porcine brain tissue and a silicone gel model material. Stapp Car Crash Journal 44: 249–260.
15. Ogden, R. W., 1972. Large Deformation Isotropic Elasticity - On the Correlation of Theory and Experiment for Incompressible Rubberlike Solids, Proceedings of the Royal Society of London. Series A, Mathematical and Physical Sciences, Vol. 326(1567): 565-584.
16. Gronenschild, E., 1997. The Accuracy and Reproducibility of a Global Method to Correct for Geometric Image Distortion in the X-ray Imaging Chain. Medical Physics 24(12): 1875-1888.
17. Gronenschild, E., 1999. Correction for Geometric Image Distortion in the X-ray Imaging Chain: Local Technique versus Global Technique. Medical Physics 26(12): 2602-2616.
18. Heikkil, J. and Silven, O., 1997. A Four-step Camera Calibration Procedure with Implicit Image Correction. The Proceedings of the Seventh IEEE Computer Society Conference on Computer Vision and Pattern Recognition: 1106-1113.
19. Slama, C. C. et al., 1980. Man. of Photogrammetry, American Society of Photogrammetry.
20. Weng, J., Cohen, P., et al. 1992. Camera Calibration with Distortion Models and Accuracy Evaluation. IEEE Transactions on Pattern Analysis and Machine Intelligence 14(10): 965-980.

21. Navab, N., Nadar, M. S., et al. 1998. 3D Reconstruction from Projection Matrices in a C-arm Based 3D-angiography System. The Proceedings of Medical Image Computing and Computer-Assisted Intervention- MICCAI, 1496: 119-129.

22. Mitschke, M. and Navab, N., 2003. Recovering the X-ray Projection Geometry for Three Dimensional Tomographic Reconstruction with Additional Sensors: Attached Camera versus External Navigation System. Medical Image Analysis 7(1): 65-78.

23. Zhang, Z. and G. Xu, 1996. Epipolar geometry in Stereo, Kluwer Academic Publishers.

24. Hartley, R. and Zisserman, A., 2003. Multiple View Geometry in Computer Vision. Cambridge University Press.

25. Zhang, Z., 1999. Flexible camera calibration by viewing a plane from unknown orientations. International Conference on Computer Vision (ICCV'99), Corfu, Greece, pages 666-673.

26. Zhang, Z., 2000. A flexible new technique for camera calibration. IEEE Transactions on Pattern Analysis and Machine Intelligence, 22(11):1330-1334.

27. Bouguet, J. Y., 1999-2008. Documentation of a Complete Camera Calibration Toolbox for Matlab. http://www.vision.caltech.edu/bouguetj/calib_doc/index.html

28. Kovesi, P. D., 2000. Phase Congruency: A Low-level Image Invariant. Psychological Research 64: 136-148.

29. Kovesi, P. D., 2003. Phase Congruency Detects Corners and Edges. The Australian Pattern Recognition Society Conference, DICTA 2003. Sydney: 309-318.

30. Kovesi, P. D. , 1996-2007. MATLAB functions for computer vision and image analysis. http://www.csse.uwa.edu.au/»pk/Research/MatlabFns/

31. Schroeder, W., et al., 2002. The visualization toolkit: an object-oriented approach to 3D (Kitware).

32. ABAQUS: ABAQUS/Standard Manual, Version 6.7.1

33. Belytschko, T., 1983. Overview of semidiscretization and time integration procedures. Computational Methods for Transient Analysis, T. Belytschko and T. J. R. Hughes. Amsterdam, Elsevier: 1-65.

34. Zienkiewicz, O.C. and Taylor, R.L., 1989. The finite element method, 4th Edition. London; New York: McGraw-Hill.

35. Cook, R. D., 1995. Finite Element Modeling for Stress Analysis. , New York: J. Wiley & Sons.